High-pressure neutron diffraction apparatus for investigating the structure of liquids under hydrothermal conditions

Burkhard Annighöfer[a], Annalisa Polidori[b,c], Anita Zeidler[b], Henry E. Fischer[c] and Philip S. Salmon[b]

[a]Université Paris-Saclay, Laboratoire Léon Brillouin, CEA-CNRS, Saclay, 91191 Gif-sur-Yvette Cédex, France; [b]Department of Physics, University of Bath, Bath, BA2 7AY, UK; [c]Institut Laue Langevin, 71 Avenue des Martyrs, F-38042 Grenoble Cédex 9, France

ARTICLE HISTORY
Compiled October 19, 2017

ABSTRACT
A high-pressure setup is described for making neutron diffraction experiments on liquids under hydrothermal conditions. Designs are given for a modified Bridgman unsupported area seal, a fluid separator that keeps apart the liquid sample and pressurising fluid, and a pressure-cell made from the null-scattering alloy $Ti_{0.676}Zr_{0.324}$. Special attention is paid to the choice of construction materials used to avoid corrosion by the liquid sample under load at elevated temperatures. The apparatus is used to investigate the structure of heavy water at pressures up to 2 kbar and temperatures up to 250 °C.

KEYWORDS
Modified Bridgman unsupported area seal; high-pressure separator; Ti-Zr high-pressure cell; neutron diffraction; structure of water

1. Introduction

Fluids such as concentrated brine under hydrothermal conditions play a key role in processes such as the creation of black smokers at mid-oceanic ridges; the sequestration of CO_2 by solubility trapping in deep aquifers and subsequent mineral trapping in carbonates; and mass transfer within the Earth's crust by hydrothermal transport and the formation of ore deposits [1–5]. Typical pressures are ∼2 kbar at the bottom of oceanic crust as compared to ∼10 kbar at the bottom of continental crust, corresponding to crust thicknesses of about 6 and 35 km, respectively [4]. The corresponding temperature depends on the location, where typical values are 150 °C for 6 km of old oceanic crust away from the volcanism of mid-oceanic ridges versus 600 °C for 35 km of continental crust. By reference to conditions at the Earth's surface, these parameters span the critical point of water at 0.22 kbar and 374 °C [6]. In research and development, such hydrothermal conditions are used for crystal growth and materials processing, where advantage is taken of the enhanced solubility of minerals in hot water (or other solvents) at high pressure [6,7]. It is therefore of interest to investigate the structure of salty water under hydrothermal conditions in order to understand,

CONTACT B. Annighöfer. Email: burkhard.annighofer@cea.fr; or P. S. Salmon, Email: p.s.salmon@bath.ac.uk

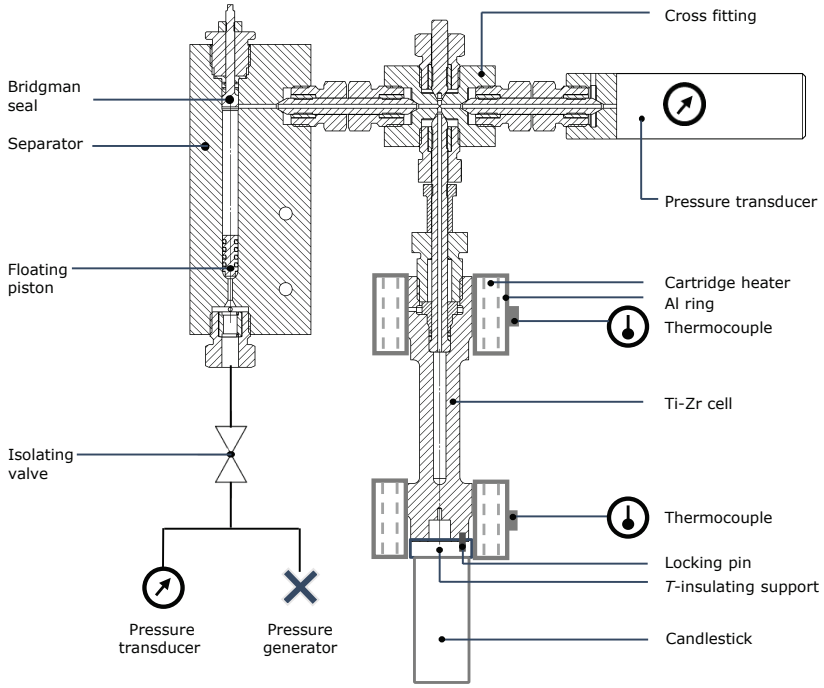

Figure 1. Schematic of the high-pressure setup used for the neutron diffraction experiment. The details of the Ti-Zr pressure cell and fluid separator are shown in Figures 2–5 and 6–7, respectively.

e.g., the speciation of ions (type and quantity of the different ionic species) and their impact on fluid properties.

The method of neutron diffraction with isotope substitution offers a means for gaining site-specific information on the structure of aqua ions, and for gauging their influence on the structure of the solvent [8,9]. The method has been used in several investigations on, e.g., aqueous solutions of NaCl [10], LiCl [11,12], $NiCl_2$ [11–13] and $NiSO_4$ [14] at high temperatures and pressures. In all of this work, the null-scattering alloy $Ti_{0.676}Zr_{0.324}$ was used to contain the sample, but there are often experimental difficulties that are associated with the corrosiveness of aqueous solutions under hydrothermal conditions [13]. In the following, we return to this issue and present new designs for a modified Bridgman unsupported area seal and a fluid separator that keeps apart the liquid sample and pressurising fluid. Special attention is paid to the choice of construction materials in order to minimise corrosion. The high-pressure setup was tested by making a neutron diffraction experiment on the structure of heavy water at pressures up to 2 kbar and temperatures up to 250 °C.

The paper is organised as follows. The high-pressure setup is described in Section 2 where detailed information is given about the $Ti_{0.676}Zr_{0.324}$ alloy used for the pressure cell (Section 2.1), the modified Bridgman unsupported area seal used for both the cell and fluid separator (Section 2.2), the pressure cell assembly and its operating conditions (Section 2.3), and the high-pressure fluid separator (Section 2.4). The neutron diffraction experiments are outlined in Section 3, and the results are given in Section 4. Conclusions are drawn in Section 5.

2. High-pressure setup

An overview of the high-pressure setup used for the neutron diffraction experiment is shown in Figure 1. For the Ti-Zr pressure-cell, we modified the design of Brian Stockford (University of Bristol) [14], which was based upon an idea by George Neilson, by closing the sample space with a modified Bridgman unsupported area seal, instead of a cone-to-cone seal. The pressure cell was mounted on a thermally insulating polyimide cap (Meldin® 7001, maximum service temperature of 315 °C) secured to the top of a candlestick made from a thin-walled stainless steel tube. A metal pin, mounted in the top of the cap, located in a hole in the bottom of the Ti-Zr cell, thus preventing rotation of the cell and ensuring that it could be mounted with a reproducible orientation. The cell was connected to a hand-driven pressure generator via a specially designed fluid-separator, and the applied pressure was monitored by transducers mounted on both the generator and sample sides of the separator. An isolating valve was placed between the pressure generator and separator in order to prevent any pressure drop that may originate from leakage in the generator. Heat was supplied to the sample by cartridge heaters embedded in aluminium ring-clamps mounted on both the top and bottom of the cell. A thermocouple was used to monitor the temperature of each of these clamps, and the power to each set of heaters was controlled separately. The candlestick, Ti-Zr pressure cell and heaters were mounted inside the vacuum bell jar of the diffractometer. All of the other components were mounted outside of this bell jar, thus ensuring that the temperature of each pressure transducer remained within an operational range.

2.1. *Ti-Zr high-pressure cell*

The pressure cell (Figure 2) was made from a null-scattering titanium-zirconium alloy with a nominal composition (in mol %) of $Ti_{0.676}Zr_{0.324}$. This composition gives a mean coherent neutron scattering length of zero: the coherent neutron scattering lengths of Ti and Zr are −3.438(2) and 7.16(3) fm, respectively, where the sign depends on whether the incident and scattered neutrons are in or out of phase [15]. The measured neutron diffraction pattern for this type of alloy should therefore be flat and featureless, provided that its components mix to form an ideal solution [16].

The Ti-Zr alloy has good corrosion resistance to aqueous solutions under high pressure and temperature conditions [17], which originates from the formation of a thin-adherent oxide-film layer on the metal surface. For zirconium, the air-formed oxide film is of thickness ∼3 nm, and is susceptible to pitting corrosion in aqueous HCl [18]. For titanium, the oxide film provides an effective barrier against chemical attack or penetration by hydrogen, but if it is destroyed by chemical attack or the corrosion caused by galvanic coupling, rapid embrittlement and cracking can occur under stress, especially at higher temperatures [19]. It is therefore important to test the corrosion resistance of the Ti-Zr alloy for a given experiment. For instance, the passive oxide film on the surface of titanium or zirconium is broken-down by a dry organic alcohol such as methanol and the surface does not re-passivate quickly, which leads to stress corrosion cracking [18–20], i.e., cracking that is induced by the combined influence of tensile stress and a corrosive environment. The use of dry methanol in a Ti-Zr pressure cell at a pressure of 9 kbar and room temperature leads to the formation of pinhole leaks and cell failure [21]. Crevice corrosion and hydrogen pickup will occur for titanium in saturated brine under appropriate temperature and pH conditions [19].

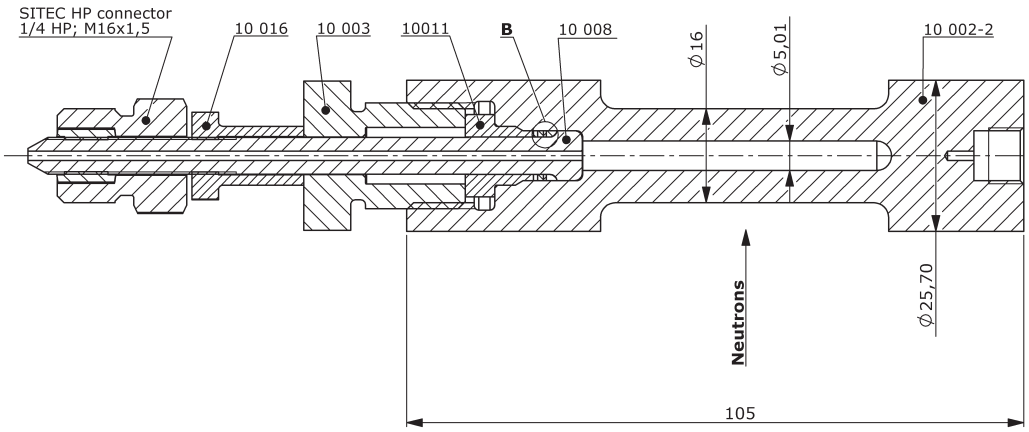

Figure 2. Cut view of the pressure cell assembly (without the heating system) showing the Ti-Zr cell (10 002-2), mushroom plug (10 008), Bridgman abutment (10 011), abutment screw (10 003), and locking nut (10 016). The marked dimensions are in units of mm. The detail B of the Bridgman seal is shown in Figure 3.

In terms of weight, the null-scattering Ti-Zr alloy has a nominal composition of 52.3 wt% Ti and 47.7 wt% Zr. Its high strength, or ability to withstand an applied stress without failure or plastic deformation, is enhanced by the addition of a small amount of oxygen (0.05–0.15 wt%), leading to a good compromise between elongation at fracture and ultimate tensile strength. In general, as the oxygen content is decreased, the strength of the alloy decreases but its toughness (ability to plastically deform without fracturing) increases. For example, a high-purity alloy with an oxygen content of 0.05 wt% will deliver at room temperature a 0.2% offset yield strength of 547–555 MPa, an ultimate tensile strength of 702–706 MPa, and an elongation at fracture of 14-21%. In comparison, the Ti-Zr alloy used for our cell had an oxygen content of 0.155 wt%, giving a measured 0.2% offset yield strength of 704–725 MPa, an ultimate tensile strength of 845–861 MPa, and an elongation at fracture of 8–13%.

Residual impurities should be kept to a minimum. For instance, hafnium is found in the same alloys as zirconium, and its content should be kept below 0.002 wt% because it absorbs neutrons and is activated by neutron irradiation [20,22,23]. Carbon, oxygen and nitrogen are among the chief impurities found in titanium [24]. All three act as interstitial solutes that dissolve preferentially in the alpha-phase to give a tradeoff between desirable and undesirable material properties, where the detrimental effects are enhanced in the presence of hydrogen. There is, however, no clear demarkation line of interstitial content that separates the good and poor material properties. In titanium, the interstitial elements strengthen the metal with little loss of ductility under tensile stress, where the different elements vary in their strengthening effect [24]. However, these interstitial elements have a deleterious effect on the metal toughness and notch sensitivity, increase its strain-rate sensitivity, produce yield-point phenomena, and decrease its machinability. The interstitial elements also lose their strengthening effect at elevated temperatures and promote embrittlement at sub-zero temperatures. In the

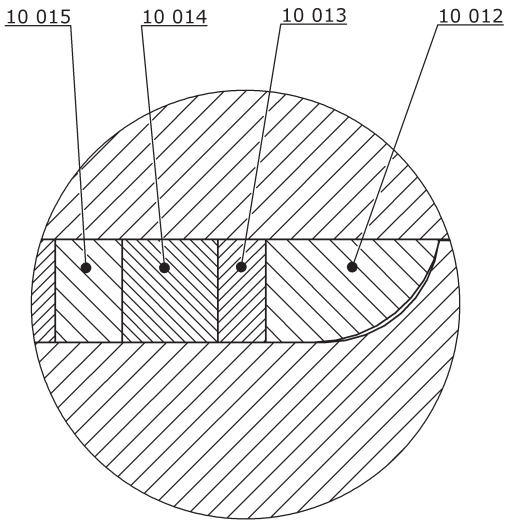

Figure 3. View of the modified Bridgman unsupported area seal (detail B in Figure 2), showing a soft central ring (10 014) that is sandwiched between two anti-extrusion rings (10 013 and 10 015), an arrangement that is in turn sandwiched between a harder shaped front-packing ring (10 012) on the mushroom-head side of the seal, and a harder back-packing ring on the opposite side of the seal (part 10 011 in Figure 2).

construction of a Ti-Zr pressure cell, a small amount of oxygen is desirable because of its strengthening effect, but impurities such as carbon, nitrogen and hydrogen should be minimised.

2.2. *Modified Brigdman unsupported area seal*

For our Ti-Zr cell (Figure 2), the bore diameter of 5 mm would lead to a Stockford cone-to-cone contact seal [14] with a circular ring-shaped sealing surface that is too large for the contact material to be easily plastified, thus limiting the maximum accessible pressure. Furthermore, the original choice of stainless steel for the cone connection with the Ti-Zr alloy could lead to galvanic corrosion (in which one metal dissolves preferentially when it is in electrical contact with another metal in the presence of an electrolyte) and concomitant stress-corrosion cracking. This corrosion can lead to leakage or failure of the pressure-cell in, e.g., experiments on electrolytes under high pressure and temperature conditions [13]. We therefore replaced the cone-to-cone seal by the modified Brigdman unsupported area seal shown in Figures 3–4. The operational principle of a Bridgman seal [25], when combined with an appropriate choice of materials, will ensure that the Ti-Zr material of the pressure vessel, and not the seal, is the weak point in the construction. The revised setup has the advantage of producing a leak-tight connection to higher pressures.

In the basic version of the Bridgman seal assembly [25], all of the material of the soft layer can be extruded if the dimensions of the seal are badly adjusted, which

Figure 4. View of the modified Bridgman unsupported area seal used for the Ti-Zr high-pressure cell during its assembly. Mounted on the mushroom plug are (from right to left) the front-packing ring, first anti-extrusion ring, soft central ring, second anti-extrusion ring, and back-packing ring. The numbered ruler markings are on the cm scale.

could lead to a pressure leak. In the modified seal, this situation is avoided by adding a suitably dimensioned anti-extrusion ring to each side of the soft central-ring in order to limit extrusion of the soft material under high pressure conditions. In addition, the seal is constructed to produce a strength cascade in which a soft middle material is surrounded by other materials with progressively increasing strengths. Under load, the soft ring will plastify first, then the anti-extrusion rings, and then the front- and back-packing rings, thus closing all of the gaps. As shown in Figure 3, there is also a difference in radius between the tip of the shaped front-packing ring (10 012) and the mushroom plug (part 10 008 in Figure 2). When pressure is applied to the mushroom plug, it will move back against the abutment screw (10 003) shown in Figure 2 and loosen the locking-nut (10 016), but the seal will prevent further motion. In consequence, the tip of the shaped front-packing ring will plastify, thus closing the gap with the mushroom plug and preventing contact of the sample with the seal.

At the Laboratoire Léon Brillouin, this modified Bridgman seal has been used to access pressures around 20 kbar at ambient temperature, with the choice of construction materials described in Section 2.4. This pressure is not the limit for the Bridgman unsupported area seal, but is determined by the ultimate tensile strength of the mushroom-plug material, the area ratio of the mushroom-head to stem, and the shaping of the transition between the mushroom-head and stem. For the latter, the radius of the junction should be as large and smooth as possible to reduce the stress concentration that originates from sectional change. According to Section 5.1.1.3 in [26], the seal will work up to fluid pressures about 20 % below the ultimate tensile strength of the plug material. Thus pressures up to 30 kbar are reachable

For our experiment, the construction materials of the modified Bridgman seal were selected to match the experimental conditions. Pure niobium was used for the soft central-ring; the copper-aluminium alloy TM® was used for the anti-extrusion rings; the nickel-based Hastelloy® C-22® (NiCr21Mo14W, UNS N06022) was used for the

harder front-packing ring on the mushroom-head side of the seal; and titanium grade 23 alloy (TiAl6V4 ELI (Extra-Low-Interstitial), UNS R56401) was used for the harder back-packing ring. The blank for the mushroom plug (part 10 008 in Figure 2) was a tube made from the high-strength nitrogen-alloyed austenitic stainless steel Sandvik HP 160, chosen because it has a higher strength, improved corrosion resistance and higher purity than the grade of austenitic stainless steel (1.4301/TP 304 or 1.4404/TP 316L) ordinarily used for this purpose. The cold-worked tube was machined to give the desired mushroom-plug shape (Figure 4).

The choice of material for closing the sample space is very important to avoid galvanic corrosion. The rate of corrosion depends on the type of electrolyte and the difference between the nobility of metals in the galvanic series, where the less noble metal is corroded preferentially. We chose Hastelloy® C-22® for the part (10 012 in Figure 3) that is in contact with the Ti-Zr alloy, because it has an electrode potential (in flowing sea water) that is similar to Ti, i.e., these metals are close to one another in the galvanic series. The front-packing ring is also in contact with the mushroom plug made from the HP 160 alloy, but the electrode potentials of these metals (in flowing sea water) are also similar.

To achieve a reliable seal, all of the sealing materials must have an elongation at fracture of more than 20%, and must not be susceptible to stress corrosion cracking. The final extrusion of the seal is determined by the manufacturing tolerance of the individual parts as well as the applied pressure. The parts were machined to give a 0.01 mm difference in diameter between the cell bore and the outer diameter of each ring. This specification ensures easy assembly (Figure 4) and the formation of a leak-tight seal at low pressures after the locking nut (part 10 016 in Figure 2) is tightened to ensure plastification of the soft central ring.

2.3. *Pressure cell assembly and operating conditions*

A 3-D representation of the pressure cell assembly, depicting the cell with its high-pressure connection and mounted heaters, is shown in Figure 5.

The yield strength σ_{Y} of the Ti-Zr alloy decreases with increasing temperature, and there is a danger that the alloy will react with gas in the atmosphere at temperatures greater than 200 °C, leading to embrittlement of the alloy and the risk of self-ignition [27]. It is therefore advisable not to exceed this temperature, and to operate the Ti-Zr high-pressure cell under vacuum. For a thick-walled cylinder under internal pressure, the yield pressure for the inner surface of the bore is given by $P_{\mathrm{Y}} = \sigma_{\mathrm{Y}} \left(K^2 - 1\right) / \sqrt{3} K^2$ [26,27], where $K = r_{\mathrm{o}}/r_{\mathrm{i}}$, r_{o} is the outer radius, and r_{i} is the inner radius. For the Ti-Zr alloy at 200 °C the 0.2% offset yield strength is 545 MPa [27], such that $P_{\mathrm{Y}} =$ 2717 bar at the most endangered cross-section of the bore where K, and hence P_{Y}, takes its minimal value (this region corresponds the bore for the Bridgman seal where $r_{\mathrm{i}} = 4.25$ mm and $r_{\mathrm{o}} = 11.5$ mm). The burst pressure was calculated to be $P_{\mathrm{burst}} = 2\sigma_{\mathrm{Y}} \ln K/\sqrt{3} = 6264$ bar at this cross-section by using the maximum distortion energy theory according to von Mises [26,28]. In order to maintain the protective oxide layer on the surface of the Ti-Zr alloy, the inner surface of the cell should not be plastified, so pressures up to 2.5 kbar should be safely achievable. Some plastifaction of the Ti-Zr is necessary in the region of the Bridgman seal, but its extent is limited by the front-packing ring (part 10 012 in Figure 3).

We note that Ti-Zr pressure cells have been operated under vacuum at temperatures up to 500°C [10,12–14,29], although little information is given about cell failure. In

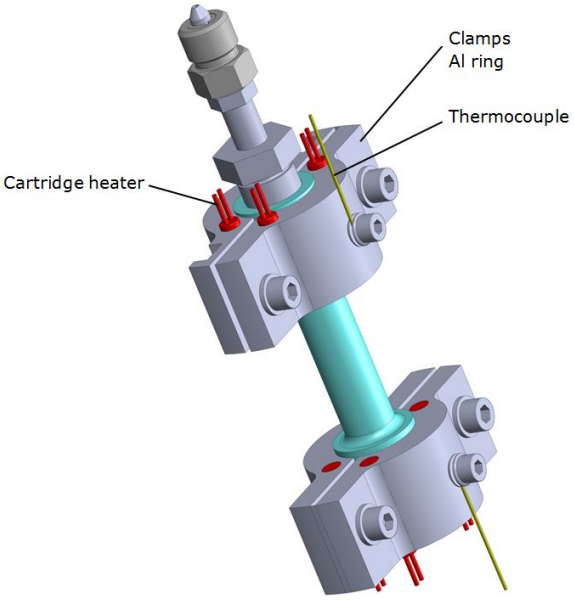

Figure 5. The assembled setup for the high-pressure cell, including the Al ring-clamps for the cartridge heaters, cartridge heaters (in red), and thermocouples (in yellow).

the case of the experiments made on supercritical water at 500°C [29], a long Ti-Zr cell was used, so that the high-pressure connection to the cell was made at a much lower temperature. In the present work, we operated the pressure cell under vacuum at temperatures up to 250 °C.

2.4. *High-pressure fluid separator*

The fluid separator ensures that the pressure transmitting medium (in our case 3M Fluorinert^{TM} liquid FC-770) does not come into contact with the sample. The design used in our setup (Figures 6 and 7) originates from the Laboratoire Léon Brillouin, where it has been extensively tested at pressures up to 7 kbar, especially in small-angle neutron scattering experiments. The fluids are separated by a floating piston (180 089) having a multiple O-ring seal (180 095), the principles of which are explained in Chapter 5 of the book by Sherman and Stadtmuller [26].

In our construction, the piston was made from the copper-beryllium alloy CuBe2 (UNS C17200) in the AT hardened condition, because of its good corrosion resistance and anti-galling properties when in contact with stainless steels. The piston operates in a cylindrical bore of diameter 6.20 mm, with a piston-to-cylinder clearance of 0.01 mm. The O-ring seals were made from the fluorocarbon elastomer Viton®/FKM with a Shore A hardness of 70. The cross-section of each O-ring groove was chosen so that the O-ring material will fill up to 93% of the grove volume. Silicon grease was used to mount the seals onto the piston.

On assembling the separator, the piston must pass through the cylinder bore for the modified Bridgman area seal and across the spout to the sample (Figure 6). The bore diameter for the Bridgman seal was therefore chosen to be 6.60 mm, larger than the diameter of the piston bore, in order to avoid damage to the uncompressed O-rings as they pass across the spout. Entry of the piston into the piston bore was aided by a

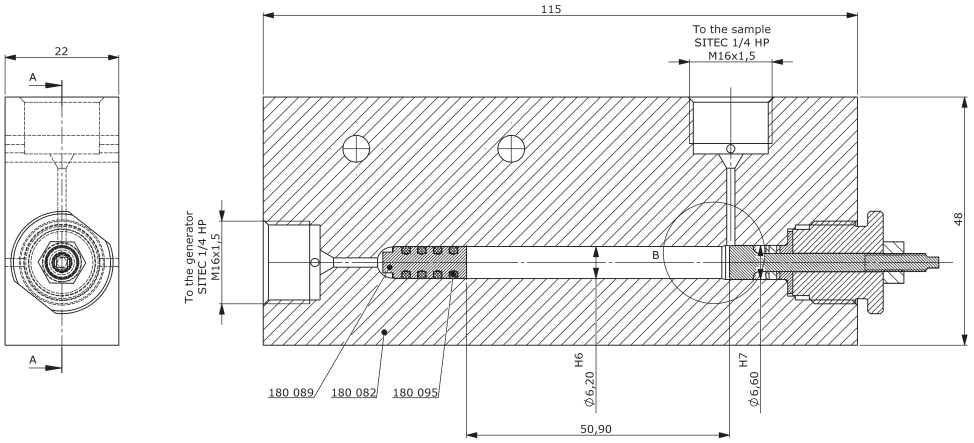

Figure 6. Cut view of the fluid separator assembly, showing the floating piston (180 089) in its starting position, the 4 O-ring piston seals (180 095), and the separator body (180 082). The marked dimensions are in mm units. The detail B of the mushroom plug of the modified Bridgman seal, at the intersection of the spout to the sample with the entrance to the piston bore, is shown in Figure 7.

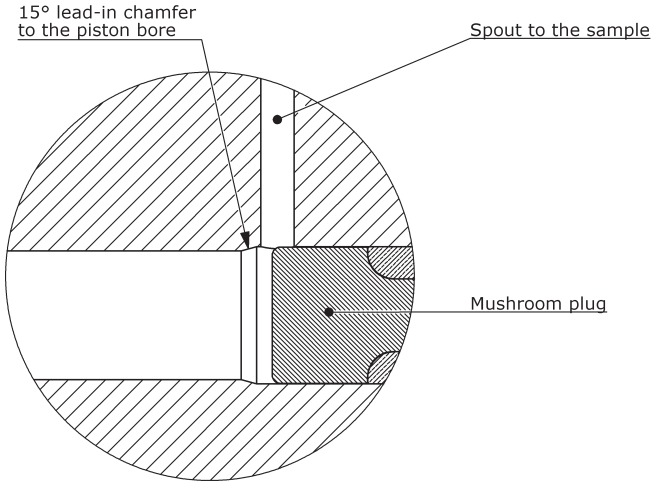

Figure 7. View at the end of the mushroom plug of the modified Bridgman seal (detail B in Figure 6), showing the spout to the sample and the 15° lead-in chamfer to the piston bore. In operation, the mushroom plug will be pushed to the right hand side by the pressure build-up in the cell as the different rings of the Bridgman seal plastify, thus opening completely the sample spout.

15° chamfer on the lead-in edge to that bore (Figure 7), and by the presence of O-ring grease. Normally, harder O-ring material is recommended for this type of application, but it fails by shearing when the piston is inserted into the piston bore.

The separator body was made from age-hardenable CarTech® Custom 465® Stainless (UNS S46500). The steel was overaged to the H1000 condition, where its strength, toughness and stress corrosion resistance are improved with respect to other generally-used high-strength precipitation-hardenable (PH) grade stainless steels. The general corrosion resistance approaches that of Type 304 stainless steel. A 5% neutral salt spray at 35 °C (as per the ASTM B117 standard) causes little or no rusting after 200 h of exposure, regardless of whether the steel is annealed or in the H900–H1100 condition. For stainless steel in particular, corrosion resistance depends on the surface roughness, and polished surfaces give the best corrosion resistance. The cylinder bore for the floating piston was therefore honed to ISO grade roughness number N3, giving a roughness value $R_\mathrm{a} = 0.1$ µm. For the steel of the separator body in its H1000 condition a transverse tensile test, with the test specimens taken transverse to the rolling direction, gave a 0.2% offset yield strength of 1496 MPa, ultimate tensile strength of 1586 MPa, and elongation at fracture of 13%. By assuming a thick-walled cylinder under internal pressure, a yield pressure $P_\mathrm{Y} = 7860$ bar was estimated for the inner surface of the bore at its most endangered cross-section, corresponding to the bore for the Bridgman seal where $r_\mathrm{i} = 3.3$ mm and $r_\mathrm{o} = 11$ mm. The burst pressure at this cross-section was calculated to be $P_\mathrm{burst} = 20798$ bar.

On the sample and pressure transmitting sides, the separator was connected to $1/4''$ outer-diameter high-pressure tubing with a maximum working pressure of 7000 bar using standard M16×1.5 cone-to-cone seals. On the sample side, the separator was sealed by a modified Bridgman unsupported area seal of the design described in Section 2.2. The materials employed in the seal construction were CarTech® Custom 465® Stainless (UNS S46500) in the H1000 condition for the mushroom plug; lead with its good corrosion resistance for the soft central-ring; pure soft copper (Cu-OFE) for the anti-extrusion rings; the aluminium bronze alloy TM® (CuAl9Ni3Fe2Mn, CW 304G from Le Bronze Industriel) for the harder front-packing ring on the mushroom-head side of the seal; and the copper-beryllium alloy CuBe2 (UNS C17200) in the AT hardened condition for the harder back-packing ring.

An alternative to CarTech® Custom 465® Stainless for the separator body and mushroom plug is the precipitation-hardened stainless steel MLX17$^{\mathrm{TM}}$ (UNS S11100) from Aubert & Duval. It has almost the same chromium and nickel content for corrosion resistance, but the elements used for precipitation hardening give improved resistance to stress corrosion cracking for steels with the same (H1000) condition [30]. Typically, the aging times at 1000 °F for Custom 465® Stainless versus MLX17$^{\mathrm{TM}}$ stainless steel are 4 h and 8 h, respectively.

For enhanced corrosion resistance, a passivation treatment for the stainless steel should be envisaged at the end of machining and after the aging process. This treatment is aimed at removing free iron or other contaminants embedded in the material surface, such as tool steel from machining or the brown oxide from prior heat treatment, and ensuring that all surfaces are protected by an oxide film. This removal of foreign particles is important because they interfere with build-up of the protective oxide layer, and thereby act as sites for corrosion attack. The passivation treatment produces an oxide film with superior corrosion resistance to the oxide film that occurs naturally on freshly machined, polished or pickled stainless steel parts that are exposed to oxygen in the atmosphere. The treatment depends on the chromium content and machinability characteristics of the stainless steel grade. For Custom 465® Stain-

less, a nitric or citric acid bath can be used for this purpose, but the latter is more environmentally friendly.

3. Neutron diffraction experiment

The pressure setup was tested by performing a diffraction experiment on heavy water (99.9 at% D, 0.01 at% H, Aldrich) using the D4c instrument at the Institut Laue-Langevin [31] with an incident neutron wavelength $\lambda = 0.4995(1)$ Å. A Rh filter was placed upstream of the monitor position in order to suppress $\lambda/2$ scattering from the Cu (220) monochromator. The apparatus shown in Figure 1 was filled with D_2O by employing a teflon micro-tube, needle and syringe, along with a procedure that was designed to avoid trapping of gas bubbles [32]. The apparatus was then mounted in the D4c vacuum bell jar, where two horizontal $^{10}B_4C$ flags mounted upstream of the sample position ensured that only the central portion of the Ti-Zr pressure cell was illuminated by the incident neutron beam.

Diffraction patterns were measured [33] for the sample in the Ti-Zr cell at a pressure of 500 bar and temperatures of 150, 200 and 250 °C, and at a pressure of 2000 bar and temperature of 250 °C. Diffraction patterns were also measured for the empty Ti-Zr cell at temperatures of 150 °C and 250 °C, a cylindrical vanadium rod of diameter 6.37(1) mm for normalisation purposes, and the empty instrument with the pressure cell removed. The relative counting times for the sample-in-cell and empty cell measurements were optimised in order to minimise the statistical error on the cell-corrected intensity [34]. Care was taken when mounting the heating clamps to ensure they were in the same position for each measurement in order to ensure that any sample dependent background, originating from secondary scattering from the clamps, did not change because of clamp re-orientation. The stability of each measurement was tested by saving the measured intensity at regular intervals, and the ratio between these intensities showed no deviation within the statistical error.

Figure 8 compares the measured diffraction patterns for the empty Ti-Zr pressure cell, a D_2O sample in this pressure cell, and the empty instrument. The diffraction pattern for the empty Ti-Zr pressure cell shows small Bragg peaks and q-dependent structure that originate from non-ideal mixing (e.g., from like-atom clustering), where the crystallites in the alloy often have preferred orientations [16]. The diffraction pattern for the empty instrument shows intensity at small q-values that originates from scattering of the direct neutron beam by the shielding of the first detector, and decreases in steps as the detector is moved in steps towards larger q-values. These artifacts, from the pressure cell and empty instrument, subtract to give a smooth diffraction pattern for the D_2O sample, which has a slope that originates from inelastic scattering [35]. The full data analysis procedure is described in [36], and the inelasticity correction was performed using the method described in [37]. The neutron scattering lengths, taking into account the isotopic enrichment of hydrogen, are $b_D = 6.661(4)$ fm and $b_O = 5.805(4)$ fm [15,38]. The number density ρ of the samples was taken from [39] (Table 1).

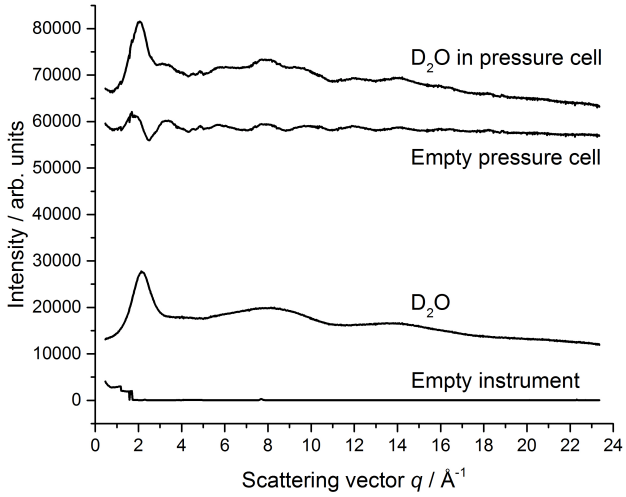

Figure 8. The measured diffraction patterns for a D_2O sample in the Ti-Zr pressure cell at a temperature of 250 °C and pressure of 2000 bar, the empty Ti-Zr pressure cell at a temperature of 250°C, the empty instrument, and the D_2O sample after subtraction of the pressure cell and background contributions. The measured data sets are shown by the solid curves with vertical error bars, where the size of an error bar is smaller than the curve thickness at most q values.

Table 1. Number density of water for the state conditions investigated during the neutron diffraction experiment.

Temperature T / °C	Pressure p / bar	Number density ρ / Å^{-3}
150	500	0.0945
200	500	0.0900
250	500	0.0845
250	2000	0.0930

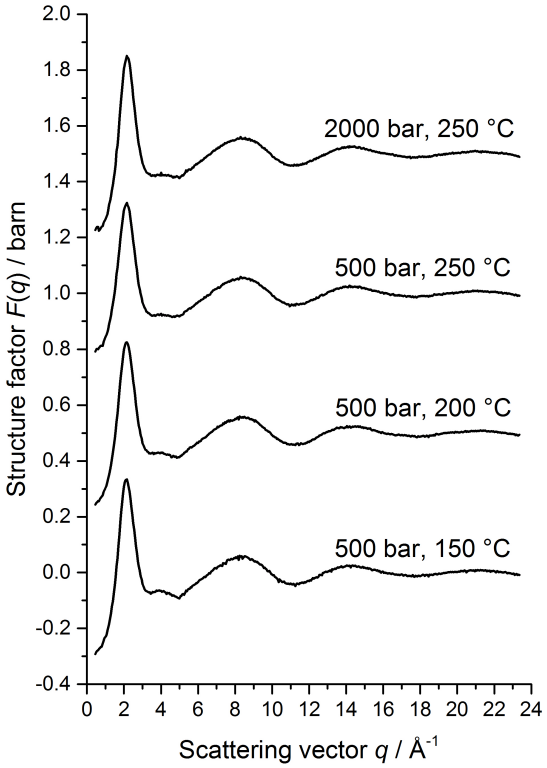

Figure 9. The measured total structure factors $F(q)$ for liquid D_2O at a pressure of 500 bar and at temperatures of 150, 200 or 250 °C, or at a pressure of 2000 bar and a temperature of 250 °C. The measured data sets are shown by the solid curves with vertical error bars, where the size of an error bar is smaller than the curve thickness at most q values.

4. Diffraction results

The information on the structure of water obtained from a neutron diffraction experiment on D_2O is given by the total structure factor [35]

$$F(q) = c_{\rm D}^2 b_{\rm D}^2 \left[S_{\rm DD}(q) - 1\right] + 2c_{\rm O}c_{\rm D}b_{\rm O}b_{\rm D}\left[S_{\rm OD}(q) - 1\right] + c_{\rm O}^2 b_{\rm O}^2 \left[S_{\rm OO}(q) - 1\right] \qquad (1)$$

where $c_{\rm D} = 2/3$ and $c_{\rm O} = 1/3$ are the atomic fractions of D and O, respectively, $S_{\alpha\beta}(q)$ is a partial structure factor, and q is the magnitude of the scattering vector. The corresponding real-space information is represented by the total pair-distribution function $G(r)$, which is obtained from the Fourier transform relation

$$G(r) = \frac{1}{2\pi^2 \rho\, r} \int_0^\infty {\rm d}q\, F(q) M(q) q \sin(qr) \qquad (2)$$

where r is a distance in real-space. $M(q)$ is a modification function that is introduced because a diffractometer can access only a finite q-range up to a maximum value $q_{\rm max}$, i.e., it imposes a step modification function $M(q) = 1$ for $q \leq q_{\rm max}$, $M(q) = 0$ for $q > q_{\rm max}$. To obtain smoother r-space functions, a Lorch [40] modification function can be employed, where $M(q) = \sin(\pi q/q_{\rm max})/(\pi q/q_{\rm max})$ for $q \leq q_{\rm max}$ and $M(q) = 0$ for $q > q_{\rm max}$.

The measured total structure factors are shown in Figure 9 and the corresponding total pair-distribution functions are shown in Figure 10. The structural features in the measured functions are characteristic of subcritical heavy water [41]. In real-space,

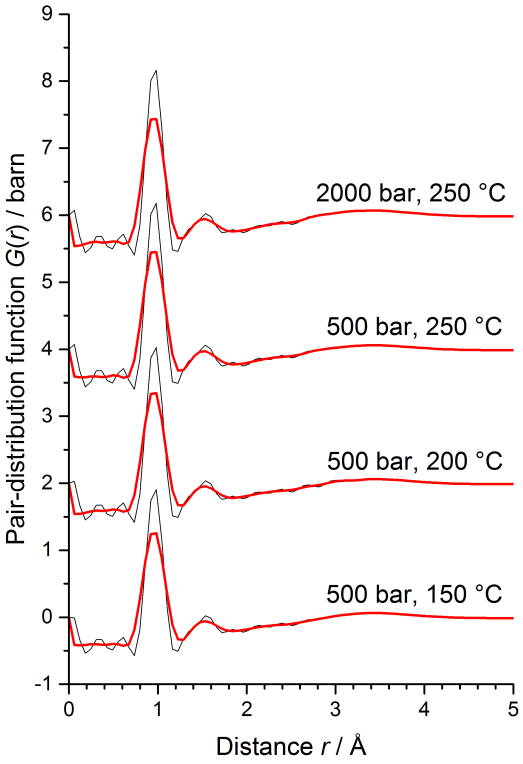

Figure 10. The total pair-distribution functions for liquid D_2O obtained by Fourier transforming the $F(q)$ functions shown in Figure 9. The dark solid (black) and light solid (red) curves were obtained by using step versus Lorch modification functions, respectively.

the first peaks at 0.96(1) Å and 1.54(1) Å originate from intra-molecular O-D and D-D correlations, respectively, but are foreshortened because of uncertainty on the inelasticity correction [42]. For example, the method of neutron diffraction with oxygen isotope substitution, in which the use of difference function methods leads to a significant reduction in the effect of inelastic scattering, gives a mean O-D distance of 0.985(5) Å [43,44]. The density-induced changes to the inter-molecular structure will be highlighted in a forthcoming paper, where the method of neutron diffraction with H/D isotope substitution is used to extract the full set of partial structure factors.

5. Conclusion

A detailed account is given of a setup developed for using neutron diffraction to measure the structure of liquids under hydrothermal conditions. Designs and construction materials are described for a modified Bridgman unsupported area seal, a fluid separator, and a $Ti_{0.676}Zr_{0.324}$ pressure cell. The setup was tested by investigating the structure of heavy water at pressures up to 2 kbar and temperatures up to 250 °C.

Acknowledgements

We are grateful to Alain Bertoni and Claude Payre for their help with the D4c experiment, to Ruth Rowlands, Stefan Klotz and Marie-Claire Bellissent-Funel for their help with earlier experimental work at the Laboratoire Léon Brillouin, and to George Neilson and Adrain Barnes for providing the Ti-Zr cell that was used in these test experiments.

Disclosure statement

No potential conflict of interest was reported by the authors.

Funding

The Bath group received support from the UK Engineering and Physical Sciences Research Council (EPSRC) via Grant No. EP/J009741/1. AZ is supported by a Royal Society–EPSRC Dorothy Hodgkin Research Fellowship, and AP was supported by a PhD studentship funded by the ILL and University of Bath.

6. References

References

[1] Wood SA. The aqueous geochemistry of the rare-earth elements and yttrium 2. Theoretical predictions of speciation in hydrothermal solutions to 350 °C at saturation water vapor pressure. Chem Geol. 1990;88:99–125.

[2] Bachu S. Sequestration of CO_2 in geological media: criteria and approach for site selection in response to climate change. Energy Convers Mgmt. 2000;41:953–970.

[3] Xu T, Apps JA, Pruess K. Numerical simulation of CO_2 disposal by mineral trapping in deep aquifers. Appl Geochem. 2004;19:917–936.
[4] Walther JV. Essentials of Geochemistry. Sudbury (MA): Jones and Bartlett; 2005.
[5] Mayanovic RA, Anderson AJ, Bassett WA, Chou I-M. On the formation and structure of rare-earth element complexes in aqueous solutions under hydrothermal conditions with new data on gadolinium aqua and chloro complexes. Chem Geol. 2007;239:266–283.
[6] Rabenau A. The role of hydrothermal synthesis in preparative chemistry. Angew Chem Int Ed Engl. 1985;24:1026–1040.
[7] Byrappa K, Yoshimura M. Handbook of hydrothermal technology: A Technology for Crystal Growth and Materials Processing. Park Ridge (NJ): Noyes; 2001.
[8] Enderby JE, Cummings S, Herdman GJ, Neilson GW, Salmon PS, Skipper N. Diffraction and the study of aqua ions. J Phys Chem. 1987;91:5851–5858.
[9] Finney JL, Soper AK. Solvent structure and perturbations in solutions of chemical and biological importance. Chem Soc Rev. 1994;23:1–10.
[10] de Jong PHK, Neilson GW. Hydrogen-bond structure in an aqueous solution of sodium chloride at sub- and supercritical conditions. J Chem Phys. 1997;107:8577–8585.
[11] Neilson GW. The effect of pressure on anionic hydration. Chem Phys Lett. 1979;68:247–250.
[12] Yamaguchi T, Ohzono H, Yamagami M, Yamanaka K, Yoshida K, Wakita H. Ion hydration in aqueous solutions of lithium chloride, nickel chloride, and caesium chloride in ambient to supercritical water. J Mol Liq. 2010;153:2–8.
[13] de Jong PHK, Neilson GW, Bellissent-Funel M-C. Hydration of Ni^{2+} and Cl^{-} in a concentrated nickel chloride solution at 100 °C and 300 °C. J Chem Phys. 1996;105:5155–5159.
[14] Howell I, Neilson GW. The coordination of Ni^{2+} in aqueous solution at elevated temperture and pressure. J Chem Phys. 1996;104:2036–2042.
[15] Sears VF. Neutron scattering lengths and cross sections. Neutron News. 1992;3:26–37.
[16] Zeidler A, Guthrie M, Salmon PS. Pressure-dependent structure of the null-scattering alloy $Ti_{0.676}Zr_{0.324}$. High Press Res. 2015;35:239–246.
[17] Neilson GW, Cummings S. Neutron diffraction studies of water and aqueous solutions under pressure. Revue Phys Appl. 1984;19:803–805.
[18] VanWinkle JA. Mechanism of the passivation of zirconium in low pH solutions. (1999). PhD thesis, Oregon Graduate Institute of Science and Technology. Scholar Archive. Paper 2528.
[19] Schweitzer PA. Metallic Materials. New York: Marcel Dekker; 2003. Chapter 21, pp 627–646.
[20] Schweitzer PA. Metallic Materials. New York: Marcel Dekker; 2003. Chapter 22, pp 647–666.
[21] Weitkamp T, Neuefeind J, Fischer HE, Zeidler MD. Hydrogen bonding in liquid methanol at ambient conditions and at high pressure. Mol Phys. 2000;98:125–134.
[22] Mackintosh WD, Jervis RE. Determination of low concentrations of hafnium in reactor-grade zirconium metal and zirconium alloys by neutron activation analysis. Analytical Chem. 1958;30:1180–1182.
[23] Yau T-L. Corrosion of zirconium. In Corrosion Engineering Handbook. Ed. Schweitzer PA. New York: Marcel Dekker; 1996. pp 195–252.
[24] Ogden HR, Jaffee RI. The effects of carbon, oxygen, and nitrogen on the mechanical properties of titanium and titanium alloys. Titanium Metallurgical Laboratory, Battelle Memorial Institute, Columbus 1, Ohio, TML Report No. 20, 1955, page 2.
[25] Bridgman PW. The technique of high pressure experimenting. Proc Am Acad Arts Sci. 1914;49:627–643.
[26] Sherman WF, Stadtmuller AA. Experimetal Techniques in High-Pressure Research. Chichester: Wiley; 1987.
[27] Klotz S. Techniques in High Pressure Neutron Scattering. Boca Raton (FL): CRC Press; 2013.
[28] Buchter HH. Apparate und Armaturen der Chemischen Hochdrucktechnik. Berlin: Sprin-

ger; 1967, page 37.
[29] Bellissent-Funel M-C, Tassaing T, Zhao H, Beysens D, Guillot B, Guissani Y. The structure of supercritical heavy water as studied by neutron diffraction. J Chem Phys. 1997;107:2942–2949.
[30] Lee EU, Taylor R, Lei C, Sanders HC. Aircraft steels. Technical Report No: NAWCADPAX/TR-2009/12, Naval Air Warfare Center Aircraft Division, Patuxent River, Maryland. 2009.
[31] Fischer HE, Cuello GJ, Palleau P, Feltin D, Barnes AC, Badyal YS, Simonson JM. D4c: A very high precision diffractometer for disordered materials. Appl Phys A. 2002;74:S160-S162.
[32] Polidori A. Structure of disordered materials: from geological fluids to network glasses. PhD Thesis, University of Bath, 2017.
[33] Annighöfer B, Fischer HE, Polidori A, Salmon PS, Zeidler A. Trial experiment using a heatable Ti-Zr pressure cell. (2016) Institut Laue-Langevin (ILL), Grenoble, France. doi:10.5291/ILL-DATA.INTER-324 http://dx.doi.org/10.5291/ILL-DATA.INTER-324
[34] Salmon PS, Zeidler A, Fischer HE. Optimizing the counting times for sample-in-container scattering experiments. J Appl Cryst. 2016;49:2249–2251.
[35] Fischer HE, Barnes AC, Salmon PS. Neutron and x-ray diffraction studies of liquids and glasses. Rep Prog Phys. 2006;69:233–299.
[36] Salmon PS, Xin S, Fischer HE. Structure of the glassy fast-ion conductor $AgPS_3$ by neutron diffraction. Phys Rev B. 1998;58:6115–6123.
[37] Zeidler A. Ordering in amorphous binary systems. PhD Thesis, University of Bath, 2009.
[38] Fischer HE, Simonson JM, Neuefeind JC, Lemmel H, Rauch H, Zeidler A, Salmon PS. The bound coherent neutron scattering lengths of the oxygen isotopes. J Phys Condens Matter. 2012;24:505105-1–505105-11.
[39] Lemmon EW, McLinden MO, Friend DG. Thermophysical Properties of Fluid Systems. In: Linstrom PJ, Mallard WG, editors. NIST Chemistry WebBook, NIST Standard Reference Database Number 69. Gaithersburg (MD): National Institute of Standards and Technology, 2017. doi:10.18434/T4D303
[40] Lorch E. Neutron diffraction by germania, silica and radiation-damaged silica glasses. J Phys C Solid State Phys. 1969;2:229–237.
[41] Bellissent-Funel M-C, Bosio L. A neutron scattering study of liquid D_2O under pressure and at various temperatures. J Chem Phys. 1995;102:3727–3735.
[42] Powells JG. The structure of the water molecule in liquid water. Mol Phys. 1981;42:757–765.
[43] Zeidler A, Salmon PS, Fischer HE, Neuefeind JC, Simonson JM, Lemmel H, Rauch H, Markland TE. Oxygen as a site specific probe of the structure of water and oxide materials. Phys Rev Lett. 2011;107:145501-1–145501-5.
[44] Zeidler A, Salmon PS, Fischer HE, Neuefeind JC, Simonson JM, Markland TE. Isotope effects in water as investigated by neutron diffraction and path integral molecular dynamics. J Phys Condens Matter. 2012;24:284126-1–284126-13.